Remote Sens. **2015**, *7*, 15140-15160; doi:10.3390/rs71115140

OPEN ACCESS

remote sensing

ISSN 2072-4292

www.mdpi.com/journal/remotesensing

Article

Inter-Band Radiometric Comparison and Calibration of ASTER Visible and Near-Infrared Bands

Kenta Obata *, Satoshi Tsuchida and Koki Iwao

National Institute of Advanced Industrial Science and Technology (AIST), Geological Survey of Japan, the Research Institute of Geology and Geoinformation, Central 7, Higashi 1-1-1, Tsukuba, Ibaraki 305-8567, Japan; E-Mails: s.tsuchida@aist.go.jp (S.T.); iwao.koki@aist.go.jp (K.I.)

* Author to whom correspondence should be addressed; E-Mail: kenta.obata@aist.go.jp; Tel.: +81-29-861-3623.

Academic Editors: Jose Moreno, Richard Müller and Prasad S. Thenkabail

Received: 28 September 2015 / Accepted: 4 November 2015 / Published: 12 November 2015

Abstract: The present study evaluates inter-band radiometric consistency across the Advanced Spaceborne Thermal Emission and Reflection Radiometer (ASTER) visible and near-infrared (VNIR) bands and develops an inter-band calibration algorithm to improve radiometric consistency. Inter-band radiometric comparison of current ASTER data shows a root mean square error (RMSE) of 3.8%–5.7% among radiance outputs of spectral bands due primarily to differences between calibration strategies of the NIR band for nadir-looking (Band 3N) and the other two bands (green and red bands, corresponding to Bands 1 and 2). An algorithm for radiometric calibration of Bands 2 and 3N with reference to Band 1 is developed based on the band translation technique and is used to obtain new radiometric calibration coefficients (RCCs) for sensor sensitivity degradation. The systematic errors between radiance outputs are decreased by applying the derived RCCs, which result in reducing the RMSE from 3.8%–5.7% to 2.2%–2.9%. The remaining errors are approximately equal to or smaller than the intrinsic uncertainties of inter-band calibration derived by sensitivity analysis. Improvement of the radiometric consistency would increase the accuracy of band algebra (e.g., vegetation indices) and its application. The algorithm can be used to evaluate inter-band radiometric consistency, as well as for the calibration of other sensors.

Keywords: ASTER; VNIR band; inter-band radiometric consistency; inter-band radiometric calibration; band translation; soil line

---

1. Introduction

The Advanced Spaceborne Thermal Emission and Reflection Radiometer (ASTER), developed by the Ministry of International Trade and Industry (METI), Japan [1], has been operated aboard the U.S. National Aeronautics and Space Administration (NASA) Earth Observation System (EOS) Terra platform for 15 years, far beyond its designed lifetime of five years. The ASTER archive contains over 2.8 million scenes [2] and has provided several global products (e.g., the ASTER Global Digital Elevation Model (GDEM)) [3] and applications, for example lithological and mineral mapping [4,5] and volcanic activity monitoring [6]. ASTER delivers 60-km swath data with resolutions of 15 m over visible and near-infrared (VNIR) bands (0.52–0.86 μm), 30 m over the shortwave infrared (SWIR) band (1.60–2.43 μm) and 90 m over the thermal infrared (TIR) band (8.125–11.65 μm). The VNIR, SWIR and TIR bands have three, six and five spectral bands, respectively. The sensor also observes backward pointing in the NIR band with a spatial resolution of 15 m for the generation of digital elevation models. Unfortunately, the temperature of the SWIR detectors began to rise due to the degradation of the detector cooler system since September 2004, and thus, the SWIR data obtained after April 2008 are invalid [7].

The radiometric calibration of ASTER, especially for the VNIR bands, including Bands 1 (green), 2 (red) and 3N (near-infrared (NIR) for nadir-looking), was implemented pre-launch, and in-flight calibration has been performed using onboard calibrators, vicarious calibration and cross-calibration. The pre-launch calibration of the bands was conducted using an integrating sphere, in which the radiance level was traceable to a primary standard copper-point blackbody [8–10]. The calibration was transferred to onboard calibration lamps and their monitoring photodiodes [10]. After launch, in-flight calibration was performed by the onboard calibrator every 33 days (originally 17 days; currently 49 days) [11]. The vicarious calibration based on a reflectance-based approach [12–16] has been conducted jointly by Saga University, the University of Arizona and the National Institute of Advanced Industrial Science and Technology, Japan (AIST), over dry lakes in Nevada, U.S.A., such as Railroad Valley Playa and Ivanpah Playa [17]. The cross-calibration with the Moderate Resolution Imaging Spectroradiometer (MODIS) onboard Terra was performed over the vicarious calibration sites [18]. The latest version of the radiometric database (DB) is ver. 4, which has been used since February 2014 for Level 1A processing [19]. A brief explanation of the calibration is provided below describing the problems addressed in this study.

The in-flight radiometric calibration of ASTER VNIR bands was achieved by onboard calibration. The radiometric calibration of Bands 1 and 2, however, was switched from onboard calibration to a coupled vicarious calibration and cross-calibration in February 2014, which is reflected in the current radiometric DB. The reason for this change was a reported discrepancy among decreasing sensor sensitivity trends with respect to the onboard calibration and the other two calibrations after approximately the 1500th day since launch [20], as well as a series of discussions in the ASTER Science Team Meeting of 2012–2014. Band 3N is primarily calibrated through onboard calibration results, in which the calibration coefficient after the 4876th day since launch is set to a constant based on the results of vicarious calibration, which exhibit a flat trend with time [19,20]. Note that the accuracy of onboard calibration would be less than that of pre-flight calibration, because the pre-flight calibration source was used to calibrate the onboard calibrators with the sensor as a transfer radiometer, and the

harsh environment of space increases the uncertainty with time of the calibrators [17,21]. Moreover, the calibrators may fail or malfunction in a space environment [17].

The present study clarifies the inter-band radiometric consistency. The ASTER Bands 1 and 2 are calibrated by vicarious calibration and cross-calibration, whereas Band 3N is primarily calibrated by onboard calibration, as mentioned above. The discrepancy in the calibration strategy would cause an inconsistency in radiometric calibration and subsequent computations of radiances across bands, because independent calibration methods may provide different values of systematic and random errors. In such a case, spectral bands output different values of radiances, even if they sense identical radiances. Specifically, the inconsistency in radiances between Bands 2 and 3N due to the use of an independent calibration strategy can impose systematic errors in computing vegetation indices (VIs) using the red and NIR bands (e.g., the normalized difference vegetation index (NDVI)) [22], and the errors can propagate into remote sensing applications, including the detection of vegetation amount and land cover classification. The evaluations of inter-band (intra-sensor) radiometric consistency and inter-band calibration are therefore a prerequisite. Inter-band radiometric calibration using a well-calibrated reference band is one calibration technique; for example, numerous studies have used deep convective clouds (DCC) as a target for the calibration, which exhibits nearly flat spectra in the VNIR band [23–26]. The inter-band calibration technique can provide relative radiometric consistency across the reference and all inter-calibrated bands, which cannot be examined/provided by other calibration methods. However, the calibration target showing flat spectra is required or we need to obtain the hyperspectral reflectances from the surface of the target for compensating the effects of the sensor's relative spectral responses (RSRs) during inter-band comparison/calibration.

The objective of the present study is to evaluate inter-band radiometric consistency on ASTER VNIR bands and to develop an algorithm for radiometric calibration of ASTER Bands 2 and 3N with reference to Band 1 in order to improve relative radiometric accuracy. The reason for selecting Band 1 as a reference is that the sensor sensitivity degradation curves for Band 1 from the three in-flight calibration methods exhibited good agreement in the early stage (from launch day to approximately the 700th day), during which onboard calibration likely worked properly. The calibration target was selected to be a dry lake in Nevada, U.S.A. (Railroad Valley Playa), because information regarding the spectral profile of the surface reflectance factor is available. The Railroad Valley Playa is one of the instrumented and reference test sites for in-flight radiometric calibration endorsed by the Committee on Earth Observation Satellites (CEOS), which is appropriate for inter-band radiometric comparison/calibration. The details of the site and data information are first introduced in Section 2, and the algorithms used for inter-band radiometric comparison and calibration for ASTER VNIR bands are presented in Section 3. Section 4 describes the results of the inter-band radiometric comparison and calibration. The uncertainty analysis of inter-band calibration is provided in Section 5, followed by the discussion and the conclusion in Sections 6 and 7, respectively.

2. Site and Data Information

2.1. Site Information

The region of interest (ROI) is located at approximately 38.505°N and 115.691°W, 1438 m above sea level over the Railroad Valley Playa [27] in central Nevada, U.S.A. (approximately 15 km by 15 km), as shown in Figure 1. The Railroad Valley Playa is endorsed as an instrumented and reference standard test site for in-flight calibration by the CEOS subgroup on the Infrared Visible Optical Sensor (IVOS) [28]. The Railroad Valley Playa is a clay-dominated dry lake and is highly homogeneous and flat, with no visible vegetation. The reflectance is high, generally exceeding 0.3, except in the blue region of the spectrum, with the SWIR region exhibiting an absorption feature. The site has a low percentage of cloud coverage and a low aerosol loading under the clear sky condition. The shape of the reflectance spectrum remains similar to that measured at different times and illumination angles, although the offset of the spectrum changes with time and illumination angles [29]. Such conditions are satisfactory for reducing the effects of atmosphere and soil reflectance variability that deteriorate inter-band radiometric comparison/calibration. The present study compares radiances from a single sensor (from the same Sun-target-sensor geometry) for the inter-band calibration, and thus, the bidirectional reflectance distribution function (BRDF) has less of an influence on the results.

2.2. ASTER Data

The ASTER data, which are radiometrically and geometrically corrected and orthorectified, are obtained from the ASTER on-demand processing service developed by AIST [30]. The data used in the present study are exactly the same as the ASTER ortho product (a standard product, L3A) from the point of view of radiometric calibration, currently provided by the Japan Space Systems (JSS) website [31], and the software for orthorectification from the AIST system is almost identical to that from JSS. The selected methods for resampling and map projection are cubic convolution and geographic projection (uniform latitude/longitude), respectively, and the ortho product with these options will be a standard product for the ASTER project (L3A), which is expected to be produced by AIST. Information on the view zenith and azimuth angles, which is necessary for input to the radiative transfer model used in this study, is missing from the data. If the ASTER pointing function is not working, these angles are assumed to be zero. Otherwise, we use the pointing angle information in the metadata in order to obtain the view zenith angle, and the view azimuth angle is roughly estimated according to the inclination of the image and pointing angle information.

The ROI was imaged 78 times under clear sky conditions, among which 17 images correspond to off-nadir viewing by the pointing function (approximately +8.6° or +20.0°). However, images with saturated pixels in ASTER Bands 1 and 2 over the ROI when the band is observed in the high-gain mode are removed from the sample, yielding 59, 73 and 78 samples for Bands 1, 2 and 3N, respectively.

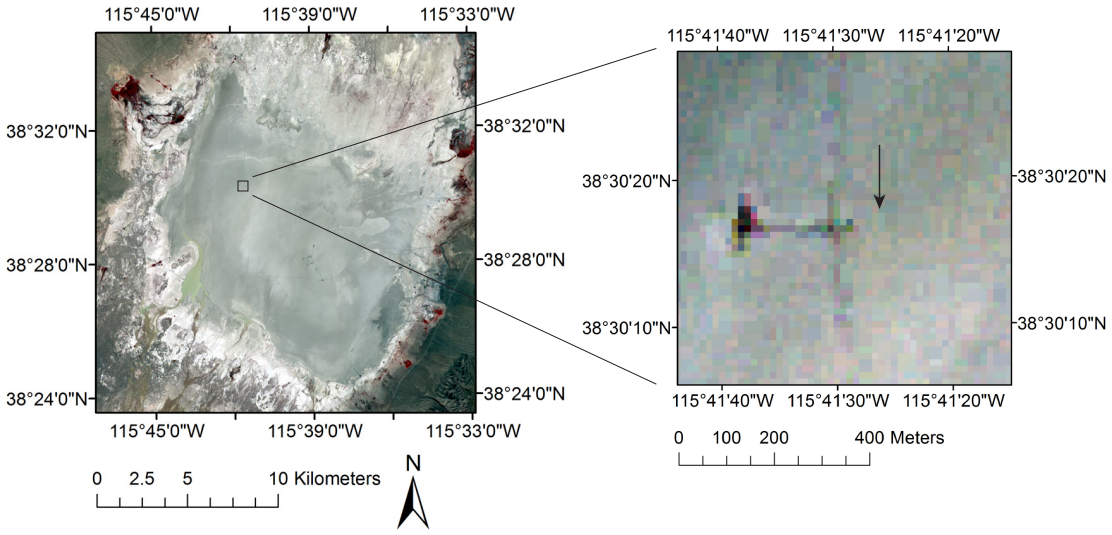

Figure 1. Image of Railroad Valley Playa in central Nevada, U.S.A., obtained by ASTER (R: Band 3N; G: Band 2; B: Band 1) and a close-up image depicting the region of interest (ROI).

3. Inter-Band Comparison and Calibration Method

The inter-band comparison and calibration in the present study are conducted in terms of the unit of spectral radiance (watts per square meter per steradian per micrometer ($W/m^2/sr/\mu m$)). The comparison algorithm consists of two parts: (1) band translation; and (2) radiometric comparison across a destination and a reference band. Similarly, the calibration algorithm consists of two parts: (1) band translation; and (2) derivation of the radiometric calibration coefficient (RCC) for the sensor sensitivity degradation of the destination band using the reference band. In band translation, the radiances of the reference band are translated into those of the destination band. The translation enables consistent comparison of "radiance outputs" among spectral bands, and spectral bands providing consistent radiances will output identical values of radiances if they sense spectrally-flat radiances.

In the present study, Bands 2 and 3N are destination bands to be compared/calibrated with reference to Band 1. The pairs of reference and destination bands are "Bands 1 and 2" and "Bands 1 and 3N". For a direct comparison between Bands 2 and 3N, we define an additional pair, "Bands 2 and 3N", in which Bands 2 and 3N are the reference and destination bands, respectively.

3.1. Band Translation

Band translation is inevitable for compensating the influences of differences in spectral responses in an effort to compare radiance outputs consistently. Band translation involves three steps: (1) the top-of-atmosphere (TOA) radiances of the reference band are first atmospherically corrected to retrieve surface reflectances by inverting a radiative transfer model; (2) the retrieved reflectance for the reference band is then translated to that of the destination band using the soil line (explained in the next paragraph); and (3) the translated surface reflectances are used as the input for the radiative transfer model to simulate the TOA radiances of the destination band. The above steps are described in Figure 2. This

approach is similar to that used for cross-sensor radiometric calibration [29], especially for radiometric cross-calibration between spectrally-matching bands of satellite sensors [32–37].

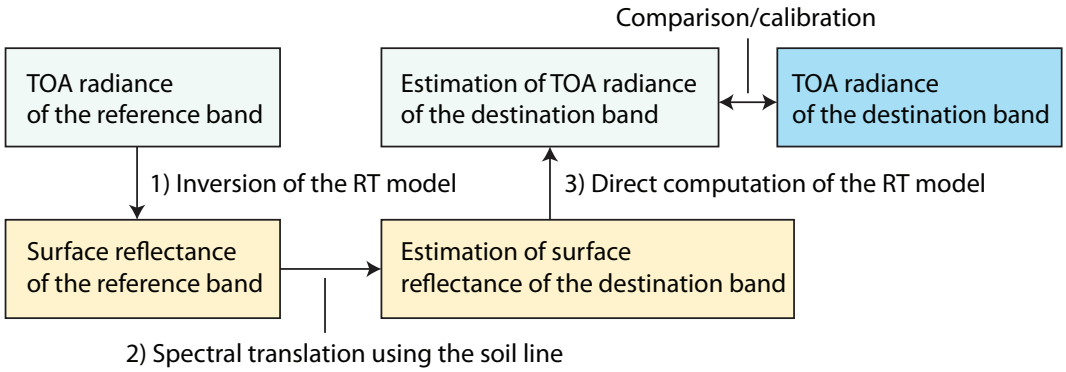

Figure 2. Band translation procedure for inter-band radiometric comparison and calibration.

Vermote and Saleous [38] used a linear relationship between the retrieved surface reflectances for a site in the Sahara Desert for converting reflectances across MODIS onboard Terra and the Advanced Very High Resolution Radiometer (AVHRR) onboard NOAA 16 in cross-calibrating the AVHRR using MODIS. In the present study, the soil line [39] refers to the linear relationship between soil reflectances of any bands in the solar-reflective range, and we used the soil line obtained from ground-measured data for translating ASTER VNIR bands.

The soil line parameters (the slope and offset) for the reference and destination bands can be derived from historical data for hyperspectral surface reflectance obtained at the past field campaigns of AIST for the ASTER vicarious calibration over the Railroad Valley Playa. The FieldSpec spectroradiometers have been used to measure reflectances of the full range in VNIR and SWIR (350 nm–2500 nm). In the field campaign, an 8° attachment is used, and the instrument is transported across the site using a 1.5-m handheld boom arm that extends the foreoptic of the instrument away from the body of the user [17]. The measurement height above the surface is approximately 1 m. The surface reflectance factor is calculated by rationing the measurements of the site to those of a reference panel. The rectangular test site is 90 m by 80 m in size, where the shorter side is perpendicular to the along-track of the Terra platform [17]. We calculated the average of the soil reflectances from the single campaign using approximately 900 measurements. The present study employs 10 average spectra of the soil reflectances obtained by performing the campaign 10 times on different dates.

In general, the soil line parameter is computed as follows: (1) The reflectances for the reference and destination bands are computed by integrating the soil spectra with the spectral response function of two bands; and (2) the reflectances for the destination band are linearly regressed using the reflectances for the reference band to provide a soil line slope and offset. Figure 3a shows 10 spectra of surface reflectance factors over the Railroad Valley Playa. Figure 3b shows a scatter plot of soil reflectances and soil lines for the reference and destination bands. The three "reference and destination" band pairs are Bands 1 and 2 (denoted by plus symbols), Bands 1 and 3N (denoted by circles) and Bands 2 and 3N (denoted by triangles). Note that the soil reflectances are assumed to describe the soil line over the reference and destination band reflectance space when the soil brightness changes (by variations in the

solar zenith angle), and so, constant values of these parameters are used elsewhere in the present study for band translation.

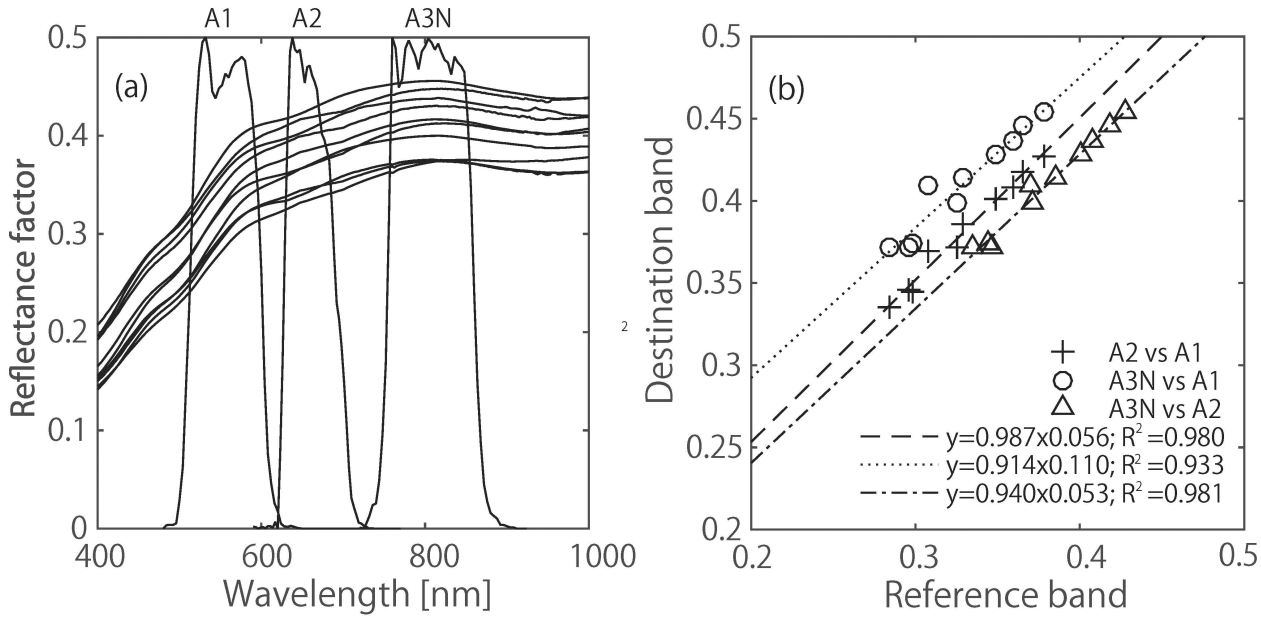

Figure 3. (**a**) Reflectance factors for the Railroad Valley Playa with the normalized relative spectral responses of ASTER Bands 1, 2 and 3N (A1, A2 and A3N). (**b**) Scatter plot of simulated surface reflectances for Band 2 *vs*. Band 1, Band 3N *vs*. Band 1 and Band 3N *vs*. Band 2, where the first band corresponds to the destination band (vertical axis) and the second band corresponds to the reference band (horizontal axis). The slope and offset of the soil lines for each band pair are shown in the legend.

The Second Simulation of a Satellite Signal in the Solar Spectrum, Vector (6SV) 1.0 Beta [40,41], is used to invert TOA radiances to the surface reflectances and to simulate TOA radiances from the surface reflectances. The exoatmospheric solar irradiance spectrum for 250–2397.5 nm stored in the original code is switched to that based on the Thuillier model of 2002 [42], which is interpolated to have an interval of 2.5 nm. The Thuillier model was recommended by CEOS for Earth Observation applications [43]. A power law distribution is chosen for representing the aerosol size distribution, which requires a parameter referred to as the Junge parameter [44]. The input parameters for 6SV are fixed, because we found that the sensitivity of the input for a radiative transfer model on band translation across ASTER VNIR bands is small enough, as reported in Section 6. This assumption is advantageous, because, in general, the real-time measurements of the atmospheric parameters for the input have not always been available over the calibration site.

The constant (average) values for the input to 6SV over the calibration site can be obtained/estimated by ground-measured data from the Aerosol Robotic Network (AERONET) [45] and satellite measurements by the Earth-Probe Total Ozone Mapping Sensor (TOMS) and Aura Ozone Monitoring Instrument (OMI). The data used to compute the constant values are based on observations made nearly simultaneously with the Terra overpass time for AERONET measurements and within a few hours of the overpass time for TOMS or OMI measurements under clear sky conditions over the test site. The average aerosol optical thickness (AOT) at 550 nm, the Junge parameter, the water vapor amount (g/cm^2)

and the total column ozone in Dobson units (DUs) are 0.064, 3.16, 0.82 and 297.7, respectively. The real and imaginary parts of the refractive index are assumed to be 1.44 and 0.005, respectively, which are empirically determined and would be appropriate for the test site [46].

3.2. Inter-Band Radiometric Comparison

The radiances for the destination band are intercompared with those for the reference band translated into the destination band using the band translation technique. The three band pairs of reference and destination, Bands 1 and 2, Bands 1 and 3N and Bands 2 and 3N, are used in the comparison.

The following statistics are computed in order to evaluate errors between the reference and destination bands. One such error is the average percentage relative difference between the radiances for the destination band ($\overline{L}_{D,i}$) and the radiances for the reference band translated into the destination band ($\hat{\overline{L}}_{D(R),i}$), which is denoted by ϵ. The subscript i identifies the data item. Another error is the root mean square error (RMSE) between $\overline{L}_{D,i}$ and $\hat{\overline{L}}_{D(R),i}$ divided by the mean of $\overline{L}_{D,i}$ as a percentage, %RMSE,

$$\epsilon = \frac{1}{N}\sum_{i=1}^{N}\left(\frac{\hat{\overline{L}}_{D(R),i} - \overline{L}_{D,i}}{\overline{L}_{D,i}}\right) \times 100 \tag{1}$$

$$\%\mathrm{RMSE} = \frac{\sqrt{\frac{1}{N}\sum_{i=1}^{N}\left(\hat{\overline{L}}_{D(R),i} - \overline{L}_{D,i}\right)^2}}{\frac{1}{N}\sum_{i=1}^{N}\overline{L}_{D,i}} \times 100 \tag{2}$$

where N is the number of data specific to the band pair of the reference and destination.

3.3. Inter-Band Radiometric Calibration

ASTER Band 1, corrected by vicarious calibration and cross-calibration, is used as the reference band for inter-band radiometric calibration, meaning that Bands 2 and 3N are radiometrically calibrated with reference to Band 1. The degradation curves for deriving the RCCs of Bands 2 and 3N are fitted using the following function, which is used to derive the RCC for ASTER vicarious calibration and cross-calibration data [19] and was presented in a study on degradation models of the ASTER VNIR sensor [47],

$$f_{D(A1)} = C_{D(A1),0}[(1.0 - C_{D(A1),1})\exp(-C_{D(A1),2} \cdot t) + C_{D(A1),1}] \tag{3}$$

where $t \in \mathbb{N}$ is the number of days since launch, $C_{D(A1),0}$ is a scaled calibration coefficient at launch day ($t = 0$), $C_{D(A1),1}$ is a coefficient for the minimum transmittances of the contamination/corrosion layer and $C_{D(A1),2}$ is a coefficient for the degradation rate. The subscript D represents the destination band, and the subscript $A1$ in parenthesis corresponds to the reference band (ASTER Band 1). A curve is fitted using a merit function, which is the sum of the squares of the difference between the fitted curve and $r_{D(A1),i}$

$$\min_{C_{D(A1),j}\in\mathbb{R}} \sum_{i=1}^{N}[r_{D(A1),i} - f_{D(A1)}(t = t_i, C_{D(A1),j})]^2 \tag{4}$$

where t_i is the date for the i-th data, j identifies the coefficients ($j = 0, 1, 2$) and $r_{D(A1),i}$ can be derived as a ratio of the radiances for the destination band, which are restored to radiances without radiometric calibration for sensor sensitivity degradation using the current RCC for the destination band ($\overline{L}^*_{D,i}$), to the radiances for the reference band, which are translated into the destination band ($\hat{\overline{L}}_{D(A1),i}$),

$$r_{D(A1),i} = \frac{\overline{L}^*_{D,i}}{\hat{\overline{L}}_{D(A1),i}} \tag{5}$$

The $\overline{L}^*_{A2,i}$ (for Band 2) is derived using the current RCC, using an equation having the same form as Equation (3), whereas $\overline{L}^*_{A3N,i}$ (for Band 3N) is derived using the current RCC, which is not represented by a mathematical function, but rather discrete values that vary with the specific term. The coefficients $C_{D(A1),0}$, $C_{D(A1),1}$ and $C_{D(A1),2}$ obtained by the fitting (the subscript D corresponds to either $A2$ or $A3N$) are used to calibrate ASTER Bands 2 and 3N.

4. Results

4.1. Inter-Band Radiometric Comparison

Inter-band radiometric comparison was performed for the three pairs of spectral bands. The numbers of band pairs were 59, 59 and 73 for Bands 1 and 2, Bands 1 and 3N and Bands 2 and 3N, respectively, due to the limitation regarding saturated pixels in Bands 1 and 2.

Figure 4a shows the ratio of the Band 2 radiance ($\overline{L}_{A2,i}$) to the Band 1 radiance that is translated into Band 2 ($\hat{\overline{L}}_{A2(A1),i}$). The ratio was close to unity in the early stage, but gradually decreased with time. The results indicate that the Band 1 radiance agreed well with that for Band 2 in the early stage, but the Band 2 radiance later decreased with time. The ϵ and %RMSE between the two radiances were 2.6 and 3.8, respectively. These values are summarized in Table 1.

The ratio of the Band 3N radiance ($\overline{L}_{A3N,i}$) to the Band 1 radiance that is translated into Band 3N ($\hat{\overline{L}}_{A3N(A1),i}$) in Figure 4b exhibits a slight increasing trend and values that are far from unity, implying that the radiance output in Band 1 is greater than that in Band 3N. The ϵ and %RMSE between the two radiances were 5.2 and 5.7, respectively, which is approximately twice the previous result.

The ratio of $\overline{L}_{A3N,i}$ to the Band 2 radiance that is translated into Band 3N ($\hat{\overline{L}}_{A3N(A2),i}$) in Figure 4c exhibits an increasing trend and tends to exceed unity at a later time. The radiance output in Band 2 was generally greater than that in Band 3N and was similar at a later time. The ϵ and %RMSE between the two radiances were 3.0 and 4.5, respectively.

The overall relationship between radiance outputs was Band 1 $>$ Band 2 $>$ Band 3N. Bands 2 and 3N were 2.6% and 5.2% smaller, respectively, on average than Band 1. The average errors (biases) were larger for the pair of Bands 1 and 3N, followed by the pair of Bands 2 and 3N and the pair of Bands 1 and 2, in that order. This indicates that, in particular, the radiance outputs of Band 3N based on onboard calibration and those based on vicarious calibration and cross-calibration are not uniform. The temporal dependency of the plots in Figure 4 implies the need for the correction of the RCCs in order for ASTER data to be radiometrically compatible among bands along time.

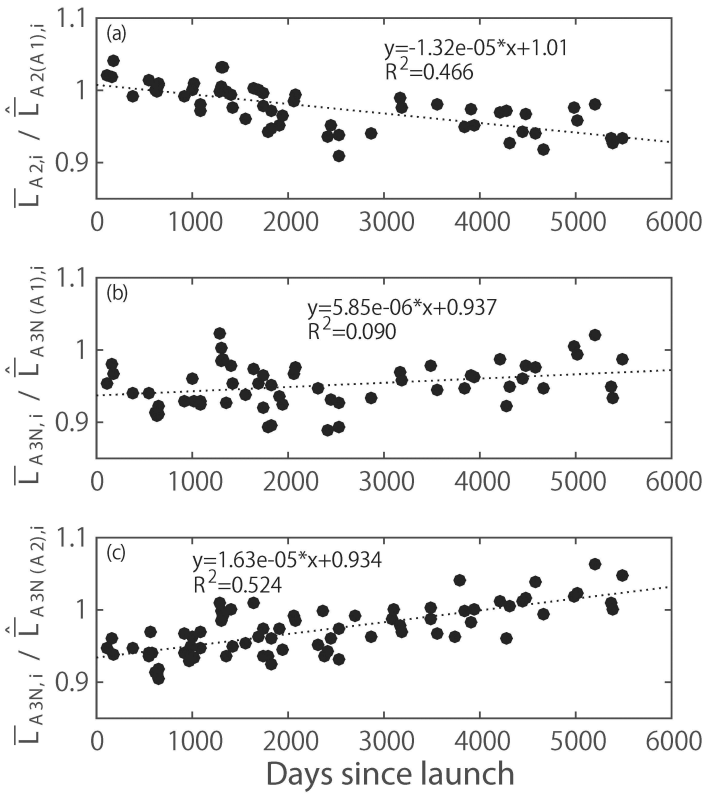

Figure 4. Results of inter-band radiometric comparison across ASTER VNIR bands, in which the effects of relative spectral responses (RSRs) are compensated using band translation. (**a**) Plot of the ratio of the Band 2 radiance to the Band 1 radiance that is translated into Band 2. (**b**) Results for Band 3N with reference to Band 1. (**c**) Results for Band 3N with reference to Band 2. The units of the slope of the regression equation are the inverse date.

Table 1. Average difference in percentage (ϵ) and %RMSE between the reference and destination bands before and after radiometric calibration of Bands 2 and 3N using Band 1 as a reference.

Reference and Destination	**Before Calibration**		**After Calibration**	
	ϵ	**%RMSE**	ϵ	**%RMSE**
A1 and A2	2.6	3.8	−0.05	2.2
A1 and A3N	5.2	5.7	0.08	2.9
A2 and A3N	3.0	4.5	−0.18	2.4

4.2. Inter-Band Radiometric Calibration

The RCCs for Bands 2 and 3N were derived using Band 1 as a reference. The curve for the current RCC for Band 1 is shown in Figure 5a. Figure 5b,c shows the results of the inter-band radiometric calibrations for Bands 2 and 3N, respectively. The ratio of the radiances for Band 2 without radiometric

calibration for sensor sensitivity degradation ($\overline{L}^*_{A2}$) to the radiances for Band 1 translated into Band 2 ($\hat{\overline{L}}_{A2(A1)}$), $r_{A2(A1),i}$, is shown in Figure 5b. The dashed and solid lines are the curve for the current RCC and that are derived from the inter-band calibration, respectively. The coefficients for the derived curve, $C_{A2(A1),0}$, $C_{A2(A1),1}$ and $C_{A2(A1),2}$, were 0.965, 0.827 and 0.001, respectively. The new curve was generally smaller than the current curve after approximately the 1000th day. The difference between the current and new curves on the 6000th day was 0.042 (4.2%). The possible reasons for this difference are the high-gain-related issue discussed in Section 6 and the uncertainty in band translation analyzed in Section 5.

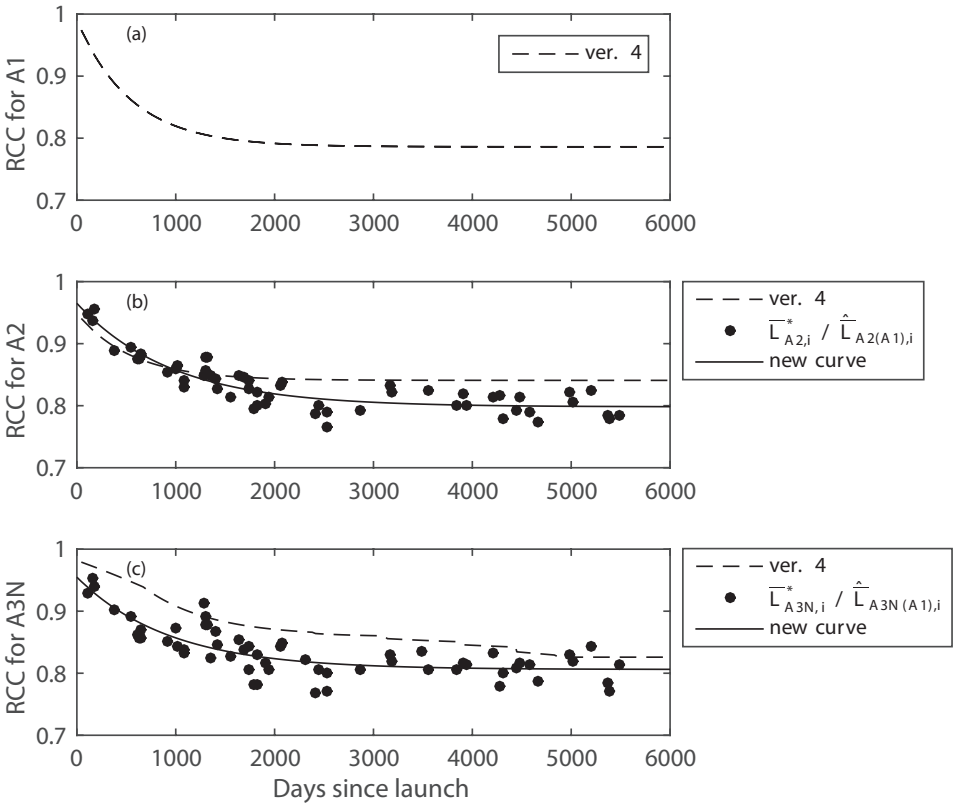

Figure 5. Results of inter-band radiometric calibration of ASTER Bands 2 and 3N using Band 1 as a reference. (**a**) Radiometric calibration coefficient (RCC) curve for Band 1. (**b**) Result of Band 2 calibration showing the ratio of the radiances for Band 2 without radiometric calibration for sensor sensitivity degradation to Band 1 radiances translated into Band 2 (denoted by dots). The dashed and solid lines correspond to the current and derived RCC curves, respectively. (**c**) Result of Band 3N calibration showing the ratio of the radiances for Band 3N without radiometric calibration for sensor sensitivity degradation to Band 1 radiances translated into Band 3N (denoted by dots). The dashed line indicates the current RCC, and the solid line corresponds to the derived RCC curve.

Figure 5c shows the ratio of radiances for Band 3N without radiometric calibration for sensor sensitivity degradation ($\overline{L}^*_{A3N}$) to the Band 1 radiances translated into Band 3N ($\hat{\overline{L}}_{A3N(A1)}$), $r_{A3N(A1),i}$, with the current RCC curve (dashed line) and the derived RCC curve (solid line). The coefficients for the new curve, $C_{A3N(A1),0}$, $C_{A3N(A1),1}$ and $C_{A3N(A1),2}$, were 0.955, 0.844 and 0.001, respectively. There

was, at most, a 6.1% difference between the current and derived RCC curves. The differences were likely caused primarily by differences in the calibration strategy (different amounts of uncertainties in the independent calibration methods for Bands 1 and 3N), in addition to the high gain-related issue and the uncertainties in band translation. The variability of the ratio in Figure 5c was larger than that in Figure 5b. These trends can be observed in the results for identical band pairs in Figure 4 (Figure 4a,b). One source of this band pair-dependent variability may be the influences of using the soil line for band translation, which is the effect of the differences between the soil line model and the actual soil spectra. The difference was slightly larger in translating Band 1 to Band 3N rather than translating Band 1 to Band 2, as shown in Figure 3b. The two RCC lines mutually converged toward the end of the period shown in Figure 5c.

The radiometric consistency of the calibrated ASTER radiances with derived RCCs for Bands 2 and 3N and the original ASTER Band 1 radiances was examined using the radiometric comparison method described in Section 3.2. The ϵ and %RMSE were, respectively, -0.05 and 2.2 for Bands 1 and 2, 0.08 and 2.9 for Bands 1 and 3N and -0.18 and 2.4 for Bands 2 and 3N, as shown in Table 1. The averages were close to zero, and the values of the %RMSE were reduced from 3.8–5.7 (original errors) to 2.2–2.9.

5. Uncertainty in Inter-Band Calibration for ASTER VNIR Bands

The source of uncertainty for intra-sensor band-to-band radiometric calibration was divided into four categories: (1) soil line influence; (2) variability in atmospheric condition; (3) accuracy of exoatmospheric solar irradiance; and (4) inherent code accuracy of a radiative transfer model. Note that the calibration uncertainty of the reference band, *i.e.*, Band 1, is not included, as inter-band calibration is performed to improve relative radiometric consistency. A sensitivity analysis is conducted in order to estimate the band pair-dependent total uncertainties calculated by combining the four sources of uncertainty.

As mentioned in the previous section, the variability in the shape of the soil spectrum with time imposes differences between the soil line and actual soil reflectance spectra, referred to as the soil line influence. We simulated 10 TOA radiances for the destination bands ($\overline{L}_D$) using the 10 soil spectra shown in Figure 3a, which does not overlap soil lines that are used for band translation, via 6SV with the average atmospheric condition. Moreover, we simulated 10 spectra of soil reflectances for the reference band, which were converted to that of the destination band using soil lines. The converted spectra were used to obtain TOA radiances for the destination band ($\hat{\overline{L}}_{D(R)}$), and the relative differences between $\hat{\overline{L}}_{D(R)}$ and $\overline{L}_D$ were computed in order to evaluate the soil line influence. The total number of differences is therefore 10. The uncertainties in the soil line influences were quantified by the standard deviation (SD) of the difference, resulting in 1.2%, 1.9% and 1.0% for Bands 1 and 2, Bands 1 and 3N and Bands 2 and 3N (reference and destination), respectively. The correlation between the soil reflectances for Bands 1 and 3N was less than those between the other band pairs, providing relatively large uncertainties for the pair of Bands 1 and 3N. The average difference (reference minus destination) was close to zero, namely, 0.07%, 0.03% and 0.06%, for each band pair.

The atmospheric condition used in our experiments was fixed. Strictly speaking, however, the atmospheric condition should be varied for each datum. Such influences for cross-calibrating

spectrally-matching bands of sensors (e.g., ASTER Band 1 and MODIS Band 4 [36]) have been small, but have yet to be evaluated for cross-calibrating spectral bands in different wavelength regions (e.g., ASTER Bands 1 and 3N). We therefore conducted a sensitivity analysis in order to infer the uncertainty due to fixing the atmospheric conditions for inter-band calibration. The data for AOT at 550 nm, the Junge parameter, the water vapor amount and the ozone column content used in Section 3.1 were used again to compute the "perturbed" input for 6SV. Three variations of four inputs, namely mean minus one sigma, mean and mean plus one sigma of the input parameters, were prepared (the statistics are shown in Table 2), and the band translation was performed using the input of $3^4 - 1 = 80$ variations ("-1" indicates the case in which neither perturbed input was excluded.) Both $\overline{L}_R$ and $\overline{L}_D$ were computed using the averaged atmospheric condition, in which the surface reflectance spectrum was the average of 10 spectra shown in Figure 3a. Afterwards, the values of $\hat{\overline{L}}_{D(R)}$ were computed using 80 combinations of perturbed inputs with $\overline{L}_R$ based on the band translation technique. The relative difference between 80 values of $\hat{\overline{L}}_{D(R)}$'s and $\overline{L}_D$ were calculated in order to evaluate the effects of atmospheric variability. The resultant uncertainties (SD) were 0.3%, 0.8% and 0.6% for Bands 1 and 2, Bands 1 and 3N and Bands 2 and 3N, respectively. The average differences (reference minus destination) were 0.01%, 0.08% and 0.07% for Bands 1 and 2, Bands 1 and 3N and Bands 2 and 3N, respectively.

Table 2. Mean and standard deviation of atmospheric parameters used as the input for the radiative transfer model in the sensitivity analysis. DUs, Dobson units, and, AOT, aerosol optical thickness.

	Mean	**SD**
AOTat 550 nm	0.064	0.042
Junge parameter	3.16	0.58
Water vapor (g/cm2)	0.82	0.44
Ozone (DUs)	297.7	28.0

Errors in exoatmospheric solar irradiance would influence the result of band translation [48]. The uncertainty in the solar irradiance in the Thuillier model of 2002 was assumed to be $<1.5\%$ over green to the NIR band based on the uncertainty analysis of the model [42]. The solar irradiances for the reference and destination bands were perturbed either -1.5% or $+1.5\%$, or were not perturbed, and the total number of combinations of perturbations, except for the case in which neither band is perturbed, was eight. Both $\overline{L}_R$ and $\overline{L}_D$ were then computed using the average atmospheric and soil conditions. The eight values of $\hat{\overline{L}}_{D(R)}$ were computed using the perturbed solar irradiance and $\overline{L}_R$, and the relative differences between the eight values of $\hat{\overline{L}}_{D(R)}$ and $\overline{L}_D$ were computed for each band pair. The uncertainties (SD) were 2.0%, 2.0% and 2.0%, respectively. The average differences (reference minus destination) were -0.06%, -0.07% and 0.16% for Bands 1 and 2, Bands 1 and 3N and Bands 2 and 3N, respectively.

The gap between the actual radiative transfer of a photon in the atmosphere and its model provides additional errors on the translation. The present study assumed an uncertainty of 1.0% or less. The inherent code accuracy of the radiative transfer code, for example the Moderate Resolution Atmospheric Transmission (MODTRAN) code (MODTRAN5) [49], is approximately $\pm 2.0\%$ in

computing radiances [50], although the value may include a certain amount of errors of the solar irradiance. The value of 2.0% is used to estimate the inherent code accuracy of 6SV. In the band translation, however, the influence of the intrinsic uncertainty in the radiative transfer model is expected to be small, because the errors in modeling TOA radiances are prone to cancellation when the radiance of the reference band is compared to those of destination bands. Therefore, in the present study, an uncertainty of 1.0% or less is assumed to be large enough.

The total uncertainties of ASTER VNIR band translation calculated by the root sum of squares were 2.6, 3.0 and 2.5, respectively, for Bands 1 and 2, Bands 1 and 3N and Bands 2 and 3N, as shown in Table 3. The influence of accuracy on solar irradiance is relatively large. The higher value of 3.0 for the pair of Bands 1 and 3N is attributed to soil line influences. The influences of variability in atmospheric conditions are smaller than the soil line and solar irradiance influences.

Table 3. Uncertainties in inter-band radiometric calibration for three band pairs of reference and destination bands. The values are percentages.

Source of Uncertainty	A1 and A2	A1 and A3N	A2 and A3N
Soil line influence	1.2	1.9	1.0
Variability in atmospheric conditions	0.3	0.8	0.6
Solar irradiance accuracy	2.0	2.0	2.0
Inherent code accuracy	<1.0	<1.0	<1.0
Root sum of squares	2.6	3.0	2.5

6. Discussion

The radiometric inter-band consistency for a single sensor, which is a focus of the present study, is crucial for remote sensing applications using the relationship between spectral bands, such as spectral vegetation indices (VIs). Currently, ASTER Bands 1 and 2 are calibrated by vicarious calibration and cross-calibration, whereas Band 3N is calibrated by onboard calibration. Specifically, the inconsistency in radiances between Bands 2 and 3N due to the use of an independent calibration strategy can impose systematic errors in computing VIs using the red and NIR bands (e.g., NDVI) [22]. The present study revealed that the same radiometric calibration strategy should be used for different spectral bands in order to increase radiometric consistency. This conclusion is based on the following: (1) the 5.7 and 4.5 %RMSE between the radiances for Bands 1 and 3N or Bands 2 and 3N obtained by inter-band radiometric comparison exceeded the uncertainty in band translation (3.0% and 2.5%), due primarily to the use of an independent calibration strategy; and (2) the distribution of points used to derive the RCC curve for Band 3N is similar to that obtained from vicarious calibration of Band 3N based on the reflectance-based method, as shown in Figure 6, which is, however, not used to derive the RCC curve for Band 3N [20].

There was a 4.2% error between the Band 2 RCCs on the 6000th day from current radiometric DB and the inter-band calibration results obtained using Band 1 as the reference, as shown in Figure 5b. The 4.2% error exceeded the intrinsic uncertainty in band translation for the pair of Bands 1 and 2 (2.6%). The dominant source of the 4.2% error is likely attributed to the high-gain-related issue for Band

1, which is briefly summarized in Appendix A. Thus, the degradation curve for Band 1 is influenced by the 2% negative error in data measured by the high-gain mode used for vicarious calibration and cross-calibration [51], and the curve will increase if the correction is applied. Therefore, the correction will subsequently shift the degradation curves derived by inter-band radiometric calibration of Band 2 (and Band 3N) upwards (Figure 5b (and Figure 5c)), which may reduce the 4.2% error to the range of the intrinsic uncertainty in band translation (2.6%) and further reduce the %RMSE between Bands 1 and 2 (and between Bands 1 and 3N). Correction of the Band 1 RCC for the high gain-related issue is thus recommended for more accurate absolute radiometric calibration of Band 1 and for comprehensive understanding of the results of inter-band radiometric calibration if Band 1 is used as the reference band.

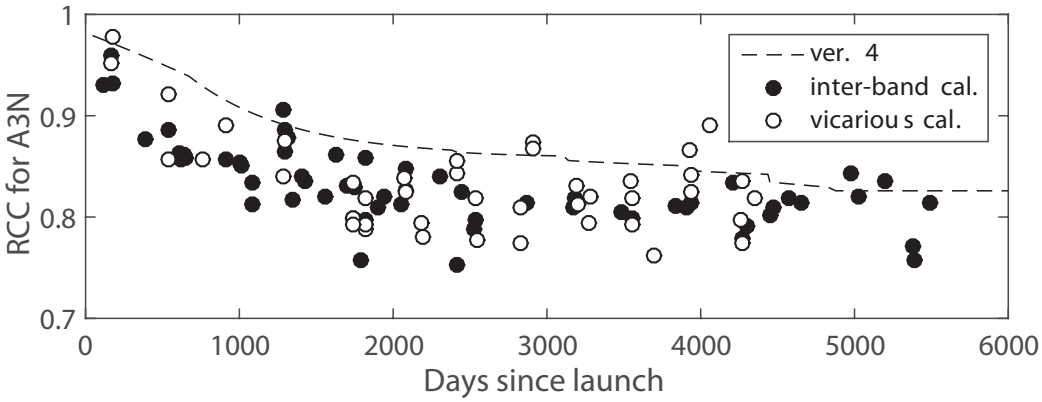

Figure 6. Comparison between the results of inter-band radiometric calibration for Band 3N with reference to Band 1 (denoted by filled circles) and the results of the vicarious calibration for Band 3N using the reflectance-based method (denoted by empty circles). The dashed line corresponds to the current RCC curve based primarily on the onboard calibration.

The uncertainties in band translation by fixing the atmospheric conditions were approximately 0.3%–0.8% (Table 3). The absolute average errors were, however, close to zero (less than 0.1%). This implies that fitted RCC curves would be reasonably less sensitive to atmospheric conditions with an increasing number of data if the input errors are normally distributed. Therefore, it is valid to say that inter-band radiometric calibration only requires the average atmospheric condition and historical data for surface reflectance measured on the ground over a dry lake, such as the Railroad Valley Playa, where the spectral shape of the surface reflectance is nearly time invariant. This is similar to findings reported in studies of cross-calibration of satellite sensors over the site [29,34,36].

The Railroad Valley Playa is preferred as the site for inter-band calibration, where the surface is highly homogeneous, flat and bright, and the percentage of aerosol loading under the clear sky condition is usually low. The spectral shape of the surface reflectance is nearly time invariant. These characteristics reduce the uncertainty in the inter-band calibration. The high expectancy of clear weather increases the opportunity of the calibration. The site for the calibration is not limited to the Railroad Valley Playa, and thus, the other calibration sites satisfying the conditions described above can be used for the inter-band calibration if the data of spectral reflectances from ground measurements are available.

7. Conclusions

ASTER Bands 1 and 2 are calibrated by vicarious calibration and cross-calibration, whereas Band 3N is calibrated by onboard calibration by the current version of the radiometric DB, ver. 4. Such a difference can cause radiometric inconsistency across bands. Inter-band radiometric comparison of ASTER VNIR bands (Bands 1, 2 and 3N) was performed in order to evaluate the influences of using independent calibration methods across bands over the Railroad Valley Playa. Moreover, an algorithm for radiometric calibration of Bands 2 and 3N with reference to Band 1 was developed in order to improve the radiometric consistency. Prior to the comparison and calibration, band translation was performed in order to compensate the effects of RSR differences, which requires the average atmospheric condition and historical data for hyperspectral surface reflectances.

The results of inter-band comparison indicate that the radiance output was not consistent across bands, and the relationship between radiance outputs becomes Band 1 $>$ Band 2 $>$ Band 3N. The radiometric performance for Band 3N was different from that for Band 1 due primarily to uncertainties in the independent calibration methods. The %RMSE between the radiances for these bands was 5.7. The 3.8 %RMSE was identified between Bands 1 and 2, which is likely influenced by the 2% error in Band 1 due to the high gain-related issue. The radiometric calibration of ASTER Bands 2 and 3N was performed using an algorithm developed in the present study with reference to Band 1, which is assumed to be more reliable. The systematic errors in radiance outputs among bands were mitigated using new RCCs, and thus, 3.8–5.7 %RMSE between radiances across bands was reduced to 2.2–2.9 %RMSE after inter-band radiometric calibration. The uncertainty in the band translation was identified to be 2.5%–3.0% in the sensitivity analysis, and residual errors computed by %RMSE (2.2–2.9) were similar to or smaller than these values for every band pair.

An improvement in the absolute radiometric accuracy for the reference band, which is Band 1 in the present study, is recommended for accurate radiometric calibration with inter-band radiometric consistency. This improvement can be achieved by solving the issue regarding the high gain mode, providing approximately a 2% error in Band 1 data.

The results in the present study revealed that the same radiometric calibration strategy should be used for different spectral bands in order to increase radiometric consistency. The algorithm based on the band translation can provide a baseline for further investigation of the intra-sensor radiometric consistency of the other sensors. We can perform inter-band radiometric comparison/calibration and its validation over other test sites by applying the historical data of the surface reflectances, including Ivanpah Playa and Alkali lake in Nevada, U.S.A, obtained in the past field campaign of AIST. Furthermore, the technique of band translation developed in this study can be applied to the spectral correction across the spectrally-matching bands in cross-calibration using different sensors.

Acknowledgments

The present study was supported by the Ministry of Economy, Trading and Industry of Japan (METI), and we are grateful to Hirokazu Yamamoto for his help in data acquisition and in preparing the manuscript. We would like to thank the ASTER onboard calibration team for providing information

on the onboard calibration. We would also like to thank Brent Holben for his effort in establishing and maintaining the AERONET site for Railroad Valley Playa.

Author Contributions

Kenta Obata and Satoshi Tsuchida designed the concept of this study. Kenta Obata developed the algorithm, performed the numerical experiment and wrote the manuscript. Satoshi Tsuchida and Koki Iwao provided help to organize the manuscript. All authors participated in the discussions on the interpretation of results and contributed to the editing and revision of the manuscript.

Conflicts of Interest

The authors declare no conflict of interest.

Appendix

A. Issues in High Gain Mode for ASTER Bands 1 and 2

The data for Bands 1 and 2 measured in the high gain mode suffered from negative errors of 2% and 7%–10%, respectively, as detected by cross-calibration with MODIS and onboard electric calibration [18,51–53]. The errors have been corrected in L1 products processed by the current radiometric DB, *i.e.*, ver. 4. However, in vicarious calibration and cross-calibration for deriving the degradation curve, negative errors of 2% in Band 1 data from the high gain mode (obtained by the previous version of the radiometric DB) were not corrected, because the errors are less than the uncertainty in the vicarious calibration (3%–5% [54]) and cross-calibration (likely more than 3% due to MODIS calibration uncertainty, RSR differences, spatial resolution difference, *etc*.). The negative errors of 7%–10% in Band 2 data for calibrations were, on the other hand, corrected for the derivation of the degradation curve.

References

1. Yamaguchi, Y.; Kahle, A.; Tsu, H.; Kawakami, T.; Pniel, M. Overview of Advanced Spaceborne Thermal Emission and Reflection Radiometer (ASTER). *IEEE Trans. Geosci. Remote Sens.* **1998**, *36*, 1062–1071.
2. Abrams, M.; Tsu, H.; Hulley, G.; Iwao, K.; Pieri, D.; Cudahy, T.; Kargel, J. The Advanced Spaceborne Thermal Emission and Reflection Radiometer (ASTER) after fifteen years: Review of global products. *Int. J. Appl. Earth Obs. Geoinf.* **2015**, *38*, 292–301.
3. ASTER GDEM Validation Team. ASTER Global Digital Elevation Model Version 2—Summary of Validation Results. 2011. Available online: https://www.jspacesystems.or.jp/ersdac/GDEM/ver2Validation/Summary_GDEM2_validation_report_final.pdf (accessed on 28 September 2015).
4. Ninomiya, Y.; Fu, B.; Cudahy, T.J. Detecting lithology with Advanced Spaceborne Thermal Emission and Reflection Radiometer (ASTER) multispectral thermal infrared "radiance-at-sensor" data. *Remote Sens. Environ.* **2005**, *99*, 127–139.

5. Van der Meer, F.D.; van der Werff, H.M.; van Ruitenbeek, F.J.; Hecker, C.A.; Bakker, W.H.; Noomen, M.F.; van der Meijde, M.; Carranza, E.J.M.; de Smeth, J.B.; Woldai, T. Multi- and hyperspectral geologic remote sensing: A review. *Int. J. Appl. Earth Obs. Geoinf.* **2012**, *14*, 112–128.
6. Carter, A.; Ramsey, M. Long-Term volcanic activity at Shiveluch Volcano: Nine years of ASTER spaceborne thermal infrared observations. *Remote Sens.* **2010**, *2*, 2571–2583.
7. ASTER Science Office. ASTER SWIR Data Status Report. 2009. Available online: http://www.science.aster.ersdac.jspacesystems.or.jp/en/about_aster/swir_en.pdf (accessed on 28 September 2015).
8. Suzuki, N.; Narimatsu, Y.; Nagura, R.; Sakuma, F.; Ono, A. Large integrating sphere of prelaunch calibration system for Japanese Earth Resources Satellite optical sensors. *Proc. SPIE* **1991**, *1493*, 48–57.
9. Thome, K.; Arai, K.; Hook, S.; Kieffer, H.; Lang, H.; Matsunaga, T.; Ono, A.; Palluconi, F.; Sakuma, H.; Slater, P.; *et al.* ASTER preflight and inflight calibration and the validation of Level 2 products. *IEEE Trans. Geosci. Remote Sens.* **1998**, *36*, 1161–1172.
10. Sakuma, F.; Ono, A.; Tsuchida, S.; Ohgi, N.; Inada, H.; Akagi, S.; Ono, H. Onboard calibration of the ASTER instrument. *IEEE Trans. Geosci. Remote Sens.* **2005**, *43*, 2715–2724.
11. Sakuma, F.; Kikuchi, M.; Inada, H.; Akagi, S.; Ono, H. Onboard calibration of the ASTER instrument over twelve years. *Proc. SPIE* **2012**, *8533*, 853305.
12. Slater, P.; Biggar, S.; Holm, R.; Jackson, R.; Mao, Y.; Moran, M.; Palmer, J.; Yuan, B. Reflectance- and radiance-based methods for the in-flight absolute calibration of multispectral sensors. *Remote Sens. Environ.* **1987**, *22*, 11–37.
13. Biggar, S.; Thome, K.; Wisniewski, W. Vicarious radiometric calibration of EO-1 sensors by reference to high-reflectance ground targets. *IEEE Trans. Geosci. Remote Sens.* **2003**, *41*, 1174–1179.
14. Thome, K.; Helder, D.; Aaron, D.; Dewald, J. Landsat-5 TM and Landsat-7 ETM+ absolute radiometric calibration using the reflectance-based method. *IEEE Trans. Geosci. Remote Sens.* **2004**, *42*, 2777–2785.
15. Naughton, D.; Brunn, A.; Czapla-Myers, J.; Douglass, S.; Thiele, M.; Weichelt, H.; Oxfort, M. Absolute radiometric calibration of the RapidEye multispectral imager using the reflectance-based vicarious calibration method. *J. Appl. Remote Sens.* **2011**, *5*, 053544.
16. Lee, S.; Jin, C.; Choi, C.; Lim, H.; Kim, Y.; Kim, J. Absolute radiometric calibration of the KOMPSAT-2 multispectral camera using a reflectance-based method and empirical comparison with IKONOS and QuickBird images. *J. Appl. Remote Sens.* **2012**, *6*, 063594.
17. Thome, K.; Arai, K.; Tsuchida, S.; Biggar, S. Vicarious calibration of ASTER via the reflectance-based approach. *IEEE Trans. Geosci. Remote Sens.* **2008**, *46*, 3285–3295.
18. Yamamoto, H.; Kamei, A.; Nakamura, R.; Tsuchida, S. Long-term cross-calibration of the Terra ASTER and MODIS over the CEOS calibration sites. *Proc. SPIE* **2011**, *8153*, 815318.
19. Tachikawa, T. ASTER Science Team Meeting. *The Earth Obs.* **2014**, *26*, 18–21.

20. Tsuchida, S.; Yamamoto, H.; Kamei, A. Long-term vicarious calibration of ASTER VNIR bands. In Proceedings of the 52nd Conference of the Remote Sensing Society of Japan, Tokyo, Japan, 23–24 May 2012; pp. 85–86. (In Japanese)
21. Slater, P.; Biggar, S.; Palmer, J.; Thome, K. Unified approach to absolute radiometric calibration in the solar-reflective range. *Remote Sens. Environ.* **2001**, *77*, 293–303.
22. Miura, T.; Huete, A.; Yoshioka, H. Evaluation of sensor calibration uncertainties on vegetation indices for MODIS. *IEEE Trans. Geosci. Remote Sens.* **2000**, *38*, 1399–1409.
23. Hagolle, O.; Goloub, P.; Deschamps, P.Y.; Cosnefroy, H.; Briottet, X.; Bailleul, T.; Nicolas, J.M.; Parol, F.; Lafrance, B.; Herman, M. Results of POLDER in-flight calibration. *IEEE Trans. Geosci. Remote Sens.* **1999**, *37*, 1550–1566.
24. Lafrance, B.; Hagolle, O.; Bonnel, B.; Fouquart, Y.; Brogniez, G. Interband calibration over clouds for POLDER space sensor. *IEEE Trans. Geosci. Remote Sens.* **2002**, *40*, 131–142.
25. Sterckx, S.; Livens, S.; Adriaensen, S. Rayleigh, deep convective clouds, and cross-sensor desert vicarious calibration validation for the PROBA-V mission. *IEEE Trans. Geosci. Remote Sens.* **2013**, *51*, 1437–1452.
26. Chen, L.; Hu, X.; Xu, N.; Zhang, P. The Application of deep convective clouds in the calibration and response monitoring of the reflective solar bands of FY-3A/MERSI (Medium Resolution Spectral Imager). *Remote Sens.* **2013**, *5*, 6958.
27. Scott, K.; Thome, K.; Brownlee, M. Evaluation of Railroad Valley playa for use in vicarious calibration. *Proc. SPIE* **1996**, *2818*, 158–166.
28. Chander, G.; Hewison, T.; Fox, N.; Wu, X.; Xiong, X.; Blackwell, W. Overview of intercalibration of satellite instruments. *IEEE Trans. Geosci. Remote Sens.* **2013**, *51*, 1056–1080.
29. McCorkel, J.; Thome, K.; Lockwood, R. Absolute radiometric calibration of narrow-swath imaging sensors with reference to non-coincident wide-swath sensors. *IEEE Trans. Geosci. Remote Sens.* **2013**, *51*, 1309–1318.
30. Kodama, S.; Yamamoto, H.; Yamamoto, N.; Kamei, A.; Nakamura, R.; Iwao, K.; Tsuchida, S. Aster digital elevation model and orthorectified images generated on the GEO Grid. In Proceedings of the 2010 IEEE International Geoscience and Remote Sensing Symposium (IGARSS), Honolulu, HI, USA, 25–30 July 2010; pp. 1418–1421.
31. Japan Space Systems. ASTER Search. Available online: http://gds.ersdac.jspacesystems.or.jp/?lang=en. (accessed on 28 September 2015).
32. Lacherade, S.; Fougnie, B.; Henry, P.; Gamet, P. Cross calibration over desert sites: Description, methodology, and operational implementation. *IEEE Trans. Geosci. Remote Sens.* **2013**, *51*, 1098–1113.
33. Bouvet, M. Radiometric comparison of multispectral imagers over a pseudo-invariant calibration site using a reference radiometric model. *Remote Sens. Environ.* **2014**, *140*, 141 – 154.
34. Teillet, P.; Barker, J.; Markham, B.; Irish, R.; Fedosejevs, G.; Storey, J. Radiometric cross-calibration of the Landsat-7 ETM+ and Landsat-5 TM sensors based on tandem data sets. *Remote Sens. Environ.* **2001**, *78*, 39 – 54.

35. Chander, G.; Mishra, N.; Helder, D.; Aaron, D.; Angal, A.; Choi, T.; Xiong, X.; Doelling, D. Applications of Spectral Band Adjustment Factors (SBAF) for cross-calibration. *IEEE Trans. Geosci. Remote Sens.* **2013**, *51*, 1267–1281.
36. Thome, K.; McCorkel, J.; Czapla-Myers, J. *In-Situ* transfer standard and coincident-view intercomparisons for sensor cross-calibration. *IEEE Trans. Geosci. Remote Sens.* **2013**, *51*, 1088–1097.
37. Mishra, N.; Haque, M.O.; Leigh, L.; Aaron, D.; Helder, D.; Markham, B. Radiometric cross calibration of Landsat 8 Operational Land Imager (OLI) and Landsat 7 Enhanced Thematic Mapper Plus (ETM+). *Remote Sens.* **2014**, *6*, 12619.
38. Vermote, E.; Saleous, N. Calibration of NOAA16 AVHRR over a desert site using MODIS data. *Remote Sens. Environ.* **2006**, *105*, 214 – 220.
39. Baret, F.; Jacquemoud, S.; Hanocq, J.F. The soil line concept in remote sensing. *Remote Sens. Rev.* **1993**, *7*, 65–82.
40. Vermote, E.; Kotchenova, S. Atmospheric correction for the monitoring of land surfaces. *J. Geophys. Res.-Atmos.* **2008**, *113*, D23S90.
41. Vermote, E.; Tanré, D.; Deuzé, J.; Herman, M.; Morcrette, J.; Kotchenova, S. Second Simulation of a Satellite Signal in the Solar Spectrum-Vector (6SV), 6S User Guide, Version 3; 2006. Available online: http://6s.ltdri.org/ (accessed on 6 November 2015).
42. Thuillier, G.; Hersé, M.; Labs, D.; Foujols, T.; Peetermans, W.; Gillotay, D.; Simon, P.; Mandel, H. The solar spectral irradiance from 200 to 2400 nm as measured by the SOLSPEC Spectrometer from the Atlas and Eureca Missions. *Solar Physics* **2003**, *214*, 1–22.
43. CEOS IVOS. CEOS Recommended Solar Irradiance Spectrum for Use in Earth Observation Applications|Infrared and Visible Optical Sensors. 2006. Available online: https://eocalibration.wordpress.com/2006/12/15/ceos-recommended-solar-irradiance-spectrum-for-use-in-earth-observation-applications/ (accessed on 28 September 2015).
44. Thome, K. Absolute radiometric calibration of Landsat 7 ETM+ using the reflectance-based method. *Remote Sens. Environ.* **2001**, *78*, 27–38.
45. Holben, B.; Eck, T.; Slutsker, I.; Tanré, D.; Buis, J.; Setzer, A.; Vermote, E.; Reagan, J.; Kaufman, Y.; Nakajima, T.; *et al*. AERONET—A Federated instrument network and data archive for aerosol characterization. *Remote Sens. Environ.* **1998**, *66*, 1–16.
46. Arai, K. Vicarious calibration of the solar reflection channels of radiometers onboard satellites through the field campaigns with measurements of refractive index and size distribution of aerosols. *Adv. Space Res.* **2007**, *39*, 13–19.
47. Tsuchida, S.; Sakuma, F.; Iwasaki, A.; Ogi, N.; Inada, H. Degradation models and functions for ASTER/VNIR sensor. In Proceedings of the 38th Conference of the Remote Sensing Society of Japan, Chiba, Japan, 20 May 2005; pp. 99–100. (In Japanese).
48. Thome, K.; Biggar, S.; Slater, P. Effects of assumed solar spectral irradiance on intercomparisons of Earth-observing sensors. *Proc. SPIE* **2001**, *4540*, 260–269.
49. Berk, A.; Anderson, G.; Acharya, P.; Shettle, E. *MODTRAN 5.2.1 User's Manual*; Spectral Sciences Inc., Air Force Research Laboratory: Burlington, MA, USA/Hanscom AFB, MA, USA, 2011.

50. Czapla-Myers, J.; McCorkel, J.; Anderson, N.; Thome, K.; Biggar, S.; Helder, D.; Aaron, D.; Leigh, L.; Mishra, N. The ground-based absolute radiometric calibration of Landsat 8 OLI. *Remote Sens.* **2015**, *7*, 600–626.
51. Sakuma, F.; Kikuchi, M.; Inada, H. Onboard electrical calibration of the ASTER VNIR. *Proc. SPIE* **2013**, *8889*, 888903.
52. Yamamoto, H.; Kamei, A.; Nakamura, R.; Tsuchida, S. Radiometric evaluation of ASTER VNIR/SWIR bands by long-term Terra ASTER/MODIS cross-calibration over the CEOS reference standard test site. In Proceedings of the 52nd Conference of the Remote Sensing Society of Japan, Tokyo, Japan, 23–24 May 2012; pp. 87–88. (In Japanese)
53. Yamamoto, H.; Koyama, T.; Nakamura, R.; Tsuchida, S. Status of ASTER/HISUI radiometric calibration—Vicarious calibration and cross-calibration. In Proceedings of the CEOS IVOS 25th Meeting, Frascati, Italy, 19–21 March 2013.
54. Biggar, S.; Slater, P.; Gellman, D. Uncertainties in the in-flight calibration of sensors with reference to measured ground sites in the 0.4–1.1 μm range. *Remote Sens. Environ.* **1994**, *48*, 245–252.